Non-destructive evaluation of concrete mixtures for direct LNG containment

Reginald B. Kogbara[1], Srinath R. Iyengar[1], Zachary C. Grasley[2],
Eyad A. Masad[1,2], Dan G. Zollinger[2]
[1]Mechanical Engineering Program, Texas A&M University at Qatar,
P.O. Box 23874, Education City, Doha, Qatar.
[2]Zachry Department of Civil Engineering, Texas A&M University,
College Station, TX 77843, USA.

Abstract

The suitability of six concrete mixtures for use in direct containment of liquefied natural gas (LNG) was assessed using nuclear magnetic resonance (NMR), x-ray computed tomography (XRCT) and acoustic emission (AE). The mixtures were prepared with river sand as fine aggregate using different coarse aggregates. The mixtures were cooled from ambient to cryogenic temperatures at a cooling rate of 3°C/min. Proton NMR measurements and XRCT imaging were carried out before and after cooling to monitor changes in porosity and pore size distribution, and internal microstructure, respectively. AE sensors monitored damage evolution during cooling and warming. NMR results indicated porosity increases of 0%, 0.3%, 1.4% and 3.3% in the non-air-entrained trap rock aggregate, limestone aggregate, sandstone aggregate and lightweight aggregate concrete mixtures, respectively. The air-entrained trap rock and limestone mixtures showed porosity increases of 0% and 1.9%, respectively. There was a strong positive correlation between AE cumulative energy and NMR porosity change. XRCT imaging generally showed no frost-induced cracking in the concrete mixtures. Thus, pore structure changes and apparent damage were in the form of microcracks less than the XRCT resolution (22 microns). The results highlight the utility of trap rock aggregate in production of durable concrete for direct LNG containment.

This is an author-created version: regkogbara@cantab.net (RB Kogbara). A definitive version was subsequently published at http://dx.doi.org/10.1016/j.matdes.2015.05.084 in *Materials & Design*, Volume 82, Pages 260 –272 (2015). The final publication is available at www.sciencedirect.com.

Non-destructive evaluation of concrete mixtures for direct LNG containment

Reginald B. Kogbara[1*], Srinath R. Iyengar[1], Zachary C. Grasley[2],

Eyad A. Masad[1,2], Dan G. Zollinger[2]

[1]Mechanical Engineering Program, Texas A&M University at Qatar,
P.O. Box 23874, Education City, Doha, Qatar.
[2]Zachry Department of Civil Engineering, Texas A&M University,
College Station, TX 77843, USA.

Abstract

The suitability of six concrete mixtures for use in direct containment of liquefied natural gas (LNG) was assessed using nuclear magnetic resonance (NMR), x-ray computed tomography (XRCT) and acoustic emission (AE). The mixtures were prepared with river sand as fine aggregate using different coarse aggregates. The mixtures were cooled from ambient to cryogenic temperatures at a cooling rate of 3°C/min. Proton NMR measurements and XRCT imaging were carried out before and after cooling to monitor changes in porosity and pore size distribution, and internal microstructure, respectively. AE sensors monitored damage evolution during cooling and warming. NMR results indicated porosity increases of 0%, 0.3%, 1.4% and 3.3% in the non-air-entrained trap rock aggregate, limestone aggregate, sandstone aggregate and lightweight aggregate concrete mixtures, respectively. The air-entrained trap rock and limestone mixtures showed porosity increases of 0% and 1.9%, respectively. There was a strong positive correlation between AE cumulative energy and NMR porosity change. XRCT imaging generally showed no frost-induced cracking in the concrete mixtures. Thus, pore structure changes and apparent damage were in the form of microcracks less than the XRCT resolution (22 microns). The results highlight the utility of trap rock aggregate in production of durable concrete for direct LNG containment.

Keywords: Acoustic emission; air-entrainment; cryogenic temperatures; microcracking, nuclear magnetic resonance; x-ray computed tomography.

* Corresponding author email: regkogbara@cantab.net. Tel: +974 4423 0289.

1.0 Introduction

Traditional liquefied natural gas (LNG) tank construction utilizes 9% Ni steel walls and floor for the inner containment tank as it has greater ductility at cryogenic temperatures (≤ -165°C) compared to normal carbon steel. Nevertheless, this construction method is becoming increasingly expensive. However, available literature on concrete properties at cryogenic temperatures shows that most properties of concrete generally improve above their ambient temperature values at cryogenic temperatures [1]. Utilization of concrete for direct LNG containment would lead to huge cost savings. Moreover, the development of the American Concrete Institute (ACI 376-11) standard on concrete structures for containment of refrigerated liquefied gases [2] may increase the impetus for tank designs utilizing concrete for primary LNG containment. Therefore, a thorough understanding of the properties of concrete related to its ability to maintain liquid tightness and structural integrity required for LNG tanks is necessary.

Concrete utilized for direct LNG containment must be dense, durable, nearly impermeable, and resistant to chemicals, with limited deflections and cracking. Its serviceability requirements must include gas-tightness to prevent leakage of LNG vapor and loss of product, and to promote durability [3]. It is evident from the foregoing that the permeability of concrete is of utmost importance in the design of concrete for use in direct LNG containment as it controls the rate by which LNG is lost from the primary container [1]. The permeability of concrete depends on the porosity, pore size distribution, pore roughness, constrictions of the pore space, and the tortuosity and connectivity of the internal pore channels [4, 5]. Moreover, the pore size distribution has a significant influence on the formation of ice and its expansion ability when concrete is cooled to cryogenic temperatures. This in turn affects the development of internal stresses in concrete due to freezing water [1]. One promising technique for quick and reliable determination of pore size distribution and porosity in porous materials like concrete is nuclear magnetic resonance (NMR). Proton NMR (also ^{1}H-NMR) is a fast, potentially non-invasive technique for the characterization of the internal structure of a porous material based on its mobile water molecule content [6]. Similarly, x-ray computed tomography (XRCT) allows for non-destructive 3D visualization of the internal microstructure of materials. XRCT is capable of viewing deeply buried microstructures that 2D surface imaging techniques – e.g. scanning electron microscopy (SEM) – may not observe. Thus, XRCT is a valuable tool used for visualization of internal microcracks and cracks in materials [7]. Furthermore, upon cracking, some of the strain energy of thermally stressed concrete is converted to wave energy, which flows through the material and is eventually released into the air making a sound [8]. This sound can be recorded by appropriately placed acoustic emission (AE) sensors. AE is a well-established, non-destructive technique for damage detection in concrete [9]. It has been successfully deployed for studying frost-induced cracking in rock and concrete [8, 10].

A ^{1}H-NMR experiment provides information on the amount of hydrogen in the pore spaces of concrete and is thus a measure of porosity as the porosity can be obtained by comparison of the ^{1}H-NMR signal of concrete with that of an equivalent volume of water. Moreover, NMR relaxation times give information on the pore size distribution of porous media as the decay of the proton (from water molecules) magnetization depends on the length scales of the pores and on the pore-fluid-grain interactions [11]. For instance, it is well known that the transverse relaxation rate ($1/T_2$) is directly proportional to the surface to volume ratio (S/V) of the pore system. Thus, if the constant of proportionality, ρ_2 – the T_2 surface relaxivity (relaxing strength of the pore surfaces) – is known alongside the T_2 relaxation time, the pore size distribution of a material can be determined. Nevertheless, the presence of paramagnetic ions in concrete components (Portland cement and aggregates) such as Fe^{3+} presents difficulties. Paramagnetic impurities may shorten relaxation times or prevent observation of some of the ^{1}H signal, as well as increase the surface relaxivity of materials [12]. Despite the challenge presented by impurities, NMR relaxometry has been deployed for different applications in cement-based materials. These include hydration kinetics of cement, compressive strength development, the physicochemical characteristics of water molecules according to their confinement level, study of the formation of the microstructure of hydration products, alongside porosity, pore size distribution and pore connectivity within the cement matrix [13-17]. Similarly, XRCT has been successfully deployed for related studies on frozen concrete mortars and cement paste. These include examination of cracking in non-air entrained mortars subjected to 35 freeze-thaw cycles between 25°C and -25°C. The study showed that cracks attempt to follow the weaker interfacial transition zone between sand and cement paste in frost-damaged mortars [18]. XRCT has also been deployed for characterization of the formation and distribution of ice crystals inside and around air voids in air-entrained hydrated cement paste. These investigations revolved around development of air-entrainment admixtures for prevention of frost damage in concrete [19].

Furthermore, as non-destructive techniques, NMR and XRCT have the advantage of investigating the internal structure of the same specimen before and after environmental changes or mechanical stress. In spite of their enormous advantages, there is a paucity of literature on the aforementioned non-destructive techniques in the study of the microstructure of concrete subjected to cryogenic temperatures, or for evaluating concrete suitability for LNG storage. The majority of previous investigations on concrete behavior for cryogenic applications have focused on mechanical and thermal properties such as compressive and tensile strengths, Young's modulus, creep, coefficient of thermal expansion (CTE) and thermal conductivity [20]. However, Bamforth [21] measured water and gas permeability at cryogenic temperatures using permeability cells, as well as porosity and pore size distribution of frozen concrete using mercury intrusion porosimetry. A similar study in this direction considered the effects of cryogenic

temperatures on hydrating white cement pastes using NMR [22]. Albeit, this study mainly investigated pore structure evolution (pore size distribution) as a function of hydration times with a view to understanding cement hydration in the lunar environment.

The present work sought to evaluate the potential of different concrete mixtures for LNG storage by complementing other assessment techniques with XRCT imaging, NMR and AE measurements of the mixtures. It builds on the findings of a previous related study [8], which showed the utility of AE for studying the potential of frost-induced microcracking in concrete during cryogenic cooling only, in relation to water and chloride permeability testing and XRCT imaging on replicate specimens. However, the present work studied the same concrete specimens before and after cryogenic cooling using NMR and XRCT, while AE measurements were made during the cooling process as well as during warming to ambient temperature. The aim of the study was to relate observed changes in porosity, pore size distribution and internal microstructure to cracking determined from cumulative energy emissions from the materials during the cooling and warming processes. It is thought that even though paramagnetic ions affect NMR relaxation times, changes in relaxation time distributions after cryogenic cooling can be attributed to pore size distribution changes since cooling is unlikely to change the paramagnetic content of a given concrete mixture. It was the object of the study to investigate the potential of the different aggregates to produce frost-damage-resistant concrete.

2. Materials and methods

2.1 Production of concrete specimens

Concrete specimens were produced using river sand as fine aggregate, and coarse aggregates with different CTE values, namely, limestone, sandstone, trap rock and TXI Streetman expanded shale lightweight aggregate. All aggregates were obtained from quarries in Texas, USA. Key physical properties and mineralogical composition of the aggregates have been detailed elsewhere [8]. Type I portland cement was used for casting of all concrete specimens. Table 1 shows the composition, mixture proportions and selected properties of the six concrete mixtures studied. Four of the six concrete mixtures were without air-entrainment, while two mixtures were air-entrained with 6% air content. Cubes (150 mm) of the non-air-entrained mixtures produced with $\leq$ 12.5 mm aggregates were initially tested after 28 and 56 days of water curing. The findings of the AE measurements, XRCT imaging and water and chloride permeability carried out have been reported elsewhere [8]. Thus, the air-entrained mixtures were produced with only limestone and trap rock aggregates, using Master Air AE 200 air-entraining admixture (*BASF*, Ohio, USA), based on the findings of the initial experiments. The grain size distributions of the aggregates used here are shown in Figure 1. The non-air-entrained mixtures had a water/cement (w/c) mass ratio of 0.42, while a w/c ratio of 0.35 was used for the air-entrained mixtures.

Table 1. Composition, mixture proportion and selected properties of the concrete mixtures

Constituent/property	Limestone mixture	Sandstone mixture	Trap rock mixture	Lightweight mixture	Air-entrained mixture	
					Limestone	Trap rock
Cement (kg/m^3)	512	512	512	512	543	543
Coarse aggregate (kg/m^3)	868	889	1056	661	868	1056
Fine aggregate (kg/m^3)	694	687	670	550	614	591
Water (kg/m^3)	215	215	215	215	188	188
Master Air AE 200 (kg/m^3)	-	-	-	-	2.9	2.4
Bulk density (kg/m^3)*	2460	2370	2650	2040	2415	2615
Compressive strength (MPa)*	36	37	40	36	29	31
% Fe_2O_3 in coarse aggregate$^+$	0.05	2.40	2.47	5.54	-	-

*Value at 28 days curing age; % Fe_2O_3 in fine aggregate$^+$ = 0.84; $^+$determined through x-ray fluorescence; % Fe_2O_3 in cement = 2.92% (product information from Qatar National Cement Company).

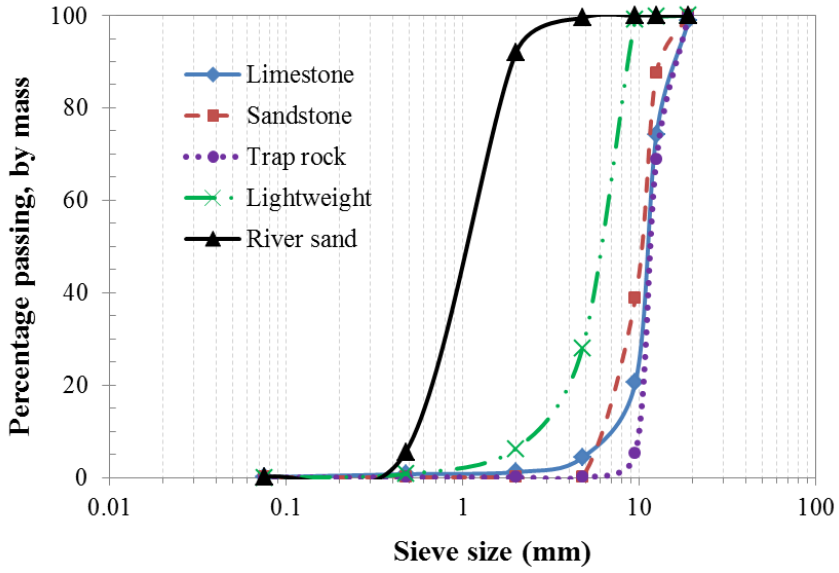

Figure 1. Grain size distribution of the coarse and fine aggregates.

The exact dimensions of the concrete specimens used were 75 mm diameter by 150 mm long for molded cylinders, and 23 mm diameter by 50 mm long for cores drilled from replicate 150 mm cubes for each mixture. The non-air-entrained and air-entrained specimens were cured under water for 365 and 28 days, respectively, before testing. The non-air-entrained specimens were all casted at the same time while the air-entrained specimens were casted 11 months later. Hence, as the difference in curing age might have some influence on experimental results, the non-air-entrained mixtures should only be compared qualitatively with the air-entrained mixtures. The 28-day compressive strengths (tested on cylinders according to ASTM C39 [23] as recommended by ACI code 376 [2]) of the non-air-entrained samples were > 34.5 MPa, while

those of the air entrained samples were > 27.6 MPa (Table 1). The strength values correspond to the minimum specified for concrete for refrigerated liquefied gases, when containing liquids (34.5 MPa), and for other reinforced concrete (27.6 MPa) in the relevant ACI code [2].

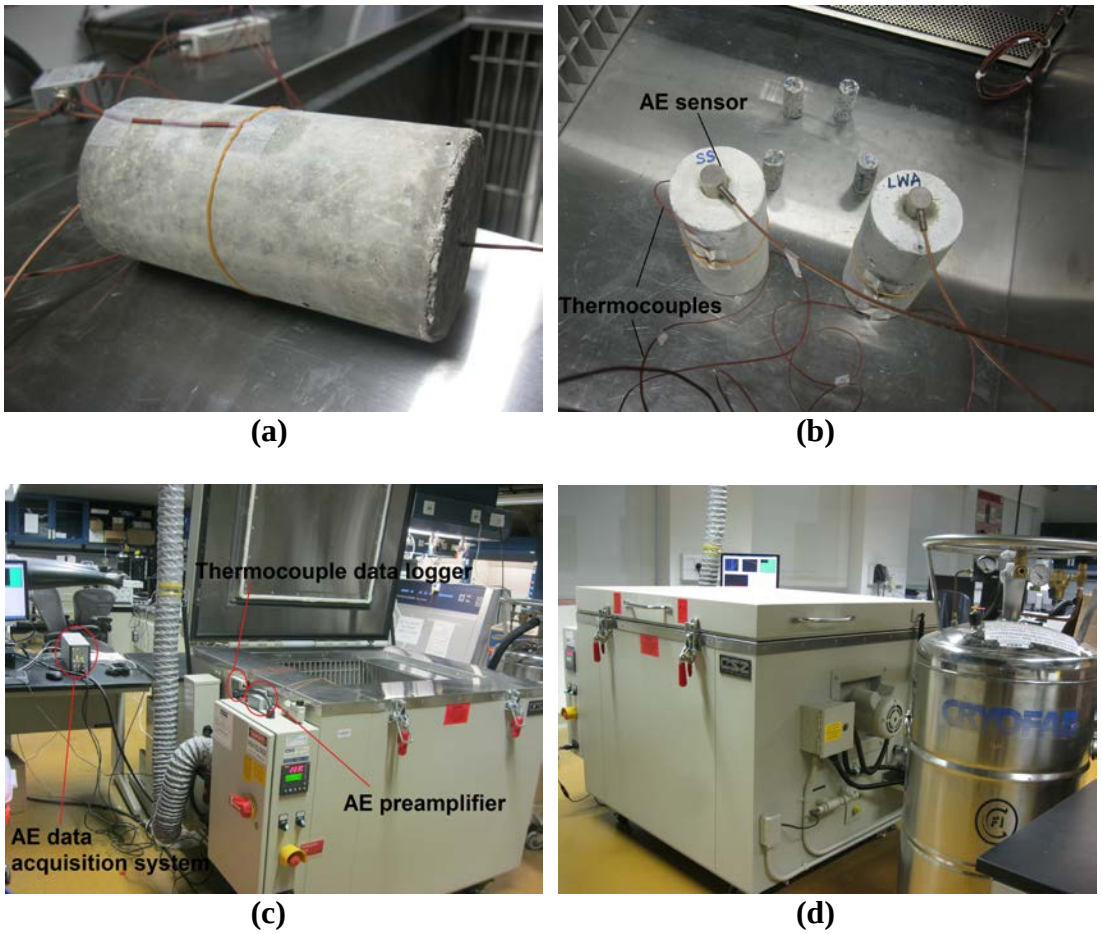

Figure 2. Experimental set-up showing arrangement of (a) & (b) thermocouples and AE sensors, and (c) & (d) temperature chamber with data acquisition system and LN2 dewar.

2.2 Cooling and warming of concrete specimens

The moist concrete specimens were placed in a *Cincinnati Sub Zero* temperature chamber and cooled from ambient to cryogenic temperatures by liquid nitrogen (LN2) injection (Figure 2). The temperature chamber is equipped with an inbuilt fan for air circulation inside the chamber. The highest possible cooling rate the temperature chamber can easily accommodate (3°C/min) was used to encourage microcracking and to better differentiate the performance of the concrete mixtures [8]. The temperature chamber was programmed to cool at the aforementioned rate down to its lowest temperature capacity (-180°C) with a guaranteed soak at that temperature until the temperature of all concrete specimens were ≤ -165°C. The temperature of the concrete

specimens was measured and monitored by Type T thermocouples, placed at a surface of the concrete polished with grade 120 abrasive paper (exposing the smaller aggregates), and also inserted into the concrete through drilled holes (Figure 2a). The thermocouples were connected to a data logger, all from *Onset Computer Corporation*, Massachusetts, USA. Thereafter, the cooling program was turned off and a single set point of ~21°C was used to warm the concrete specimens back to ambient temperature. The warming process was not programmed at a certain rate as the study focused on cryogenic cooling, since in practice, most LNG storage tanks do not undergo thermal cycling [1, 20]. This is in contrast to the procedure employed in Kogbara et al. [8], who studied the behavior of some of the mixtures here during cryogenic cooling, wherein the temperature chamber was simply cooled to -165°C. Upon warming to ambient temperature, concrete specimens for NMR measurements were re-saturated, while those for XRCT imaging were air-dried prior to imaging.

2.3 *NMR measurements*

NMR measurements were carried out on two replicate 23 mm diameter concrete cores for each of the concrete mixtures, before and after cryogenic cooling. The measurements were performed with a 2 MHz rock core analyzer using a 54 mm probe (Magritek, Wellington, New Zealand). The NMR system uses a heater to keep the magnet temperature at 30°C for field stability.

2.3.1 *Determination of porosity and pore size distribution*

The NMR instrument measures the volume of pores in a saturated cylindrical core, which in combination with bulk volume measurement of the core and a known volume of the saturation fluid, is used to calculate porosity. In an NMR experiment, a saturated sample is placed in a magnetic field; it is then excited with a series of radio frequency (RF) pulses. After each RF pulse, a small RF signal or echo is generated by the nuclei within the fluid, which is recorded as a train of echoes with a defined spacing, known as the echo time. The signal amplitude that makes up the echo train decays away with one or more relaxation times (T_2) that are characteristic of the fluid and its environment. The initial amplitude of the echo signal indicates the total amount of fluid in the sample. The relaxation time distribution gives information about the environment of the fluid, such as the pore size distribution in the sample [24].

A water-saturated concrete core covered with plastic cling wrap (to prevent moisture loss) was measured using the NMR instrument calibrated with 20 ml of tap water and correction for background signal. The bulk water T_2 was found to be ~ 3,000 ms. The Carr-Purcell-Meiboom-Gill (CPMG) sequence was used to measure T_2, with 100 µs echo time, inter-experimental delay time of 6,500 ms and 200 scans. The CPMG decay was analyzed with a Lawson and Hanson non-negative least square fit method using Prospa software (Magritek, New Zealand). A suitable

smoothing parameter was chosen, which gives a chi-squared close to the ideal value specified by the data, and prevents misplaced residual and data-noise statistics curves, and oscillations in the residuals curve. The software then outputs in excel format the cumulative porosity of the sample alongside the T_2 distribution. The logarithmic mean of the T_2 distribution, which represents the mean pore size, was used for comparison of average pore sizes before and after cryogenic cooling according to the equation

$$T_{2LM} = 10^{(\log_e T_2)} = 10^{\left(\frac{\sum_{i=1}^{n} a_i \log_e T_{2i}}{\sum_{i=1}^{n} a_i}\right)}, \quad (1)$$

where, T_{2LM} is the logarithmic mean T_2, T_{2i} and a_i are the relaxation times and intensities, respectively, in the relaxation time distribution.

2.3.2 *Estimation of surface relaxivity*

As mentioned previously, the surface relaxivity (ρ) is required alongside T_2 relaxation time for estimation of pore sizes. The presence of paramagnetic ions in concrete affects accurate determination of the parameter. It is currently unclear whether the presence of paramagnetic ions increases surface relaxivity by the same order of magnitude it decreases relaxation time. Nevertheless, the surface relaxivity of the different concrete mixtures in this work has been estimated in order to provide some idea of the pore sizes in the concrete specimens. Surface relaxivity was determined following the method described by Slijkerman and Hofman [25]. This entailed performing T_2 decay measurements in a fixed gradient field for two different echo times, which allows the extraction of surface relaxivity by modelling the effect of restricted diffusion, using the relation

$$\frac{1}{T_{2D}} = \frac{1}{T_{2S}} + \frac{D_0\left(1-\alpha\frac{1}{\rho T_{2S}}\sqrt{D_0 T_e}\right)\gamma^2 G^2 T_e^2}{12}, \quad (2)$$

where, T_{2D} is T_2 decay in a gradient field due to the combined effect of diffusion decay and surface relaxation decay; T_{2S} is the surface relaxation time; D_0 is the bulk diffusion coefficient; α is a constant equal to 0.2223; ρ is the surface relaxivity; T_e is the echo time; γ is the proton gyromagnetic ratio (= 2.675 x 10^8 rad $s^{-1}T^{-1}$) and G is the sensed field gradient.

T_2 decay measurements were performed on the concrete cores in a gradient of 34 G/cm (i.e. 0.34 T/m) at echo times of 0.5 and 2 ms at 2 MHz. The water diffusion coefficient was determined in

a separate NMR diffusion (pulsed gradient spin echo – PGSE) experiment as 2.73 x 10^{-9} m^2/s. The logarithmic mean T_{2D} at both echo times determined above was used in Equation (2). The surface relaxivity was then determined from the solution of the resulting simultaneous equations. The measurements were also carried out on sandstone and river sand samples as a check for the method since the surface relaxivity of both materials have been documented in several works [26-28].

2.4 *AE monitoring of concrete specimens*

A Vallen AMSY-6 multichannel AE measurement system (Vallen System GMBH, Germany) was employed for monitoring of damage accumulation events (hits) during cooling and warming of the concrete specimens. The AE acquisition device is equipped with two AEP4 preamplifiers with a gain of 34 dB and a frequency range of 25–850 kHz. Pancom P15 sensors were coupled to the top of two 75 mm diameter cylindrical concrete specimens from different mixtures using a high vacuum sealing compound, HIVAC-G (*Shin Etsu*, Japan), in a given cooling and warming run. These provided AE hits to the preamplifiers. One sensor was used for each specimen (Figure 2b). The sensors are specially designed for composite applications. The resonant frequency is 150 kHz and the case material is stainless steel. It has been shown that several commercially available sensors with similar characteristics are rugged enough and have sufficient fidelity to be used in a cryogenic environment [29]. The detailed procedure for the AE data acquisition and post-processing of acquired data is documented elsewhere [8].

2.5 *Microstructural examination*

The internal microstructure of the same 23 mm diameter by 50 mm long concrete core from each of the six mixtures was observed before and after cryogenic cooling using a MicroXCT-400 equipment (*Carl Zeiss Microscopy, GmbH,* Jena, Germany). The concrete cores used here were replicates of those used in the NMR measurements. During the CT scanning, a maximum electron acceleration energy of 140 kV was used with a HE #1 filter and the system acquired 2,500 projection images in approximately 2 hours 15 minutes. A Macro-70 (0.4X) detector was used, the detector-rotating axis (RA) distance was 28.3 mm, while the x-ray source-RA distance was 120 mm. The same procedure was used for all concrete cores. *ImageJ*, a public domain software, was employed for further image processing. During image processing, raw 16-bit CT data were converted to 8-bit gray scale images. The slices of the frozen specimen of a given mixture were then transformed (rotated) to match the corresponding slices of the unfrozen specimen, where necessary. There were no further adjustments to the brightness and contrast of the converted images to avoid distortion of the details captured.

3. Results and discussion

3.1 NMR results

The T_2 distributions of the different concrete mixtures are shown together with the cumulative porosities in Figure 3 and Figure 4. Table 2 shows the logarithmic mean T_2 of the relaxation time distributions. It also shows the surface relaxivity determined for the different concrete mixtures and the materials used as a check for the method of determination. In the T_2 distributions, areas higher than zero (peaks) represent pores of different sizes. The first and second peaks, which are present in all mixtures, are for the gel and capillary pores, respectively. Peaks beyond the second peak represent larger pores, cracks and very large pores. The air-entrained limestone mixture apparently showed a lower porosity compared to the corresponding non-air-entrained mixture, contrary to the higher porosity associated with air-entrainment. This is because the former did not achieve complete saturation like the latter since entrained air bubbles do not readily become saturated. Further, the rate at which an aggregate can absorb water is inversely proportional to the size of the pores [30]. The former had a much higher mean pore size than the latter (Table 2). The T_2 distributions here are generally similar to those of Diaz-Diaz et al [16], in which the T_2 values of gel pores of portland cement concrete incorporating gravel and river sand with w/c ratios of 0.3 and 0.6 were around 0.1 ms and 0.2 ms, respectively (Figures 3 and 4).

The logarithmic mean T_2 data shows that there was no change in the pore size distribution of the non-air-entrained limestone and trap rock concrete mixtures as well as the air-entrained trap rock mixture (Table 2). However, there were increases in the logarithmic mean T_2 of the non-air-entrained sandstone and lightweight concrete mixtures, and the air-entrained limestone concrete mixture. The increase in logarithmic mean T_2 suggests mean pore size increase by a factor of approximately 1.5 for the sandstone and lightweight mixtures, and 2 for the air-entrained limestone mixture (Table 2). The same trend is also apparent in the cumulative porosity data, in which the trap rock concrete mixtures, with and without air-entrainment, showed no increase in cumulative porosity after cryogenic cooling. There was a 0.3% increase in the cumulative porosity of the non-air-entrained limestone mixture, which is within the error margin. Hence, there was effectively no increase in the logarithmic mean T_2. In contrast, the sandstone and lightweight mixtures indicated 1.4% and 3.3% cumulative porosity increases, respectively. The air-entrained limestone mixture indicated 1.9% increase in porosity (Figures 3b, 3d and 4b). The generation of interconnected pores and pockets of microcracks during cryogenic cooling and warming probably engendered the porosity and mean pore size increases in the sandstone and lightweight mixtures. Sandstone and lightweight aggregates exhibit significant internal moisture movement, which causes disruptive volume changes [31]. On one hand, the expansion force associated with transformation of water into ice during cryogenic cooling could lead to

generation of larger pores as many smaller pores interconnect. On the other hand, the number of smaller pores increases such that some microcracks exist independently. This is in line with the findings of a recent study on variation of concrete pores during freezing using XRCT [32].

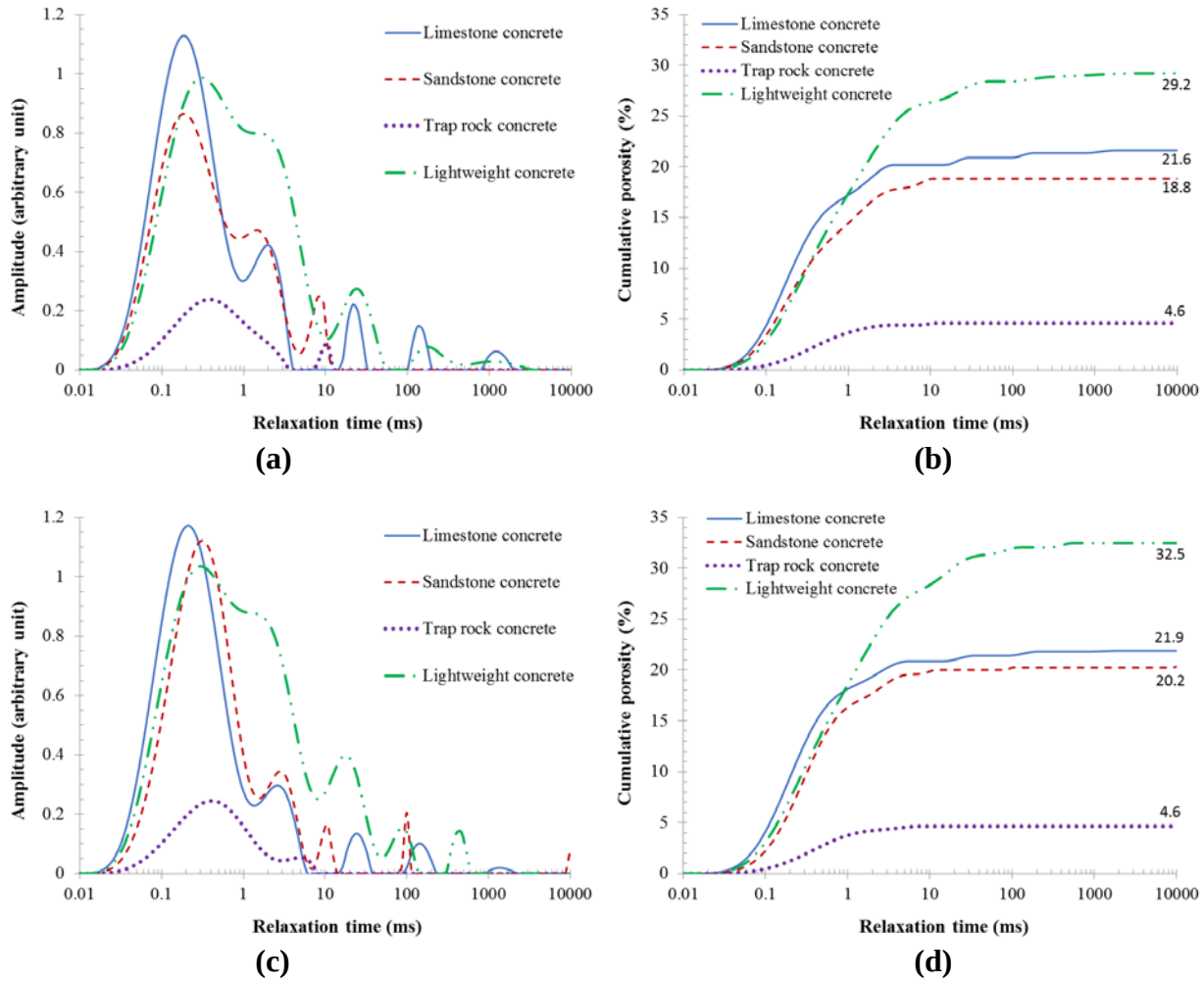

Figure 3. T_2 distribution and cumulative porosity of the non-air-entrained concrete mixtures, (a) and (b) before cryogenic cooling, (c) and (d) after cryogenic cooling.

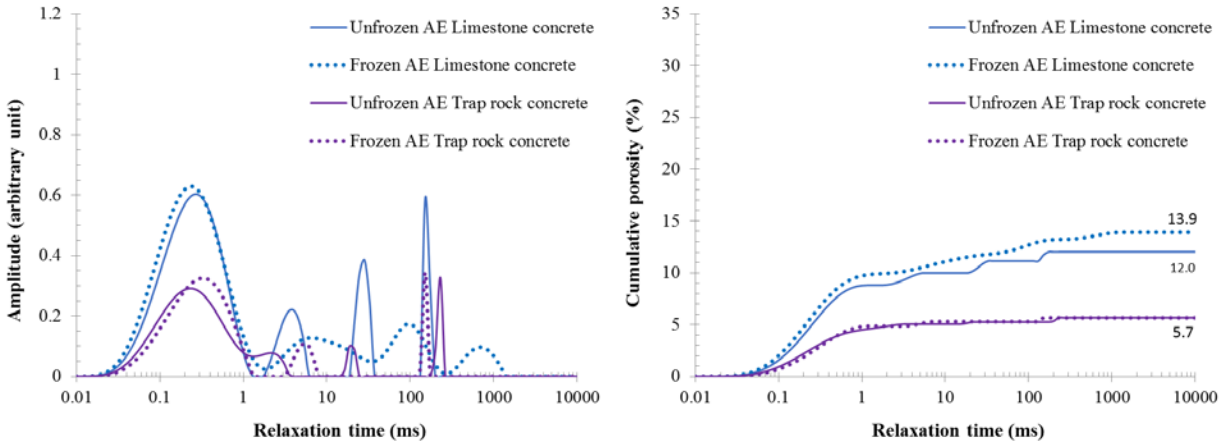

(a) (b)

Figure 4. (a) T_2 distribution and (b) cumulative porosity of the air-entrained concrete mixtures before and after cryogenic cooling.

Table 2. Logarithmic mean T_2 and surface relaxivity of the specimens

Specimen	Logarithmic mean T_2 (ms)*		Surface relaxivity (μm/s)
	Before cryogenic cooling	After cryogenic cooling	
Limestone concrete	0.1	0.1	4.7
Sandstone concrete	0.1	0.15	4.9
Trap rock concrete	0.2	0.2	4.8
Light weight concrete	0.7	1.0	5.4
AE limestone concrete	0.5	1.0	4.7
AE trap rock concrete	0.2	0.2	4.5
Sandstone	-	-	9.3
River sand	-	-	3.0

*These are for the relaxation-time distributions in Figures 3 and 4; AE: air-entrained

The above results are consistent with previous investigations in which the non-air-entrained limestone and trap rock mixtures with no effective mean pore size changes showed very little or no increase in water permeability after cryogenic cooling. Whereas, there was significant increase in the permeability of the sandstone and lightweight mixtures, which showed increases in mean pore sizes [8]. Hence, the aforementioned permeability results support the NMR assessment of porosity and mean pore size changes as well as microcracking. Especially, as it has been shown that microcracking can increase the porosity, and hence change permeability of cement-based materials by about one order of magnitude [33]. The relative contribution of the different types and sizes of pores to permeability is beyond the scope of this paper. The poor

performance of the air-entrained limestone mixture compared to the non-air-entrained mixture is probably due to the unsuitability of the large aggregate sizes used for air-entrained concrete (see Figure 1). This resulted in a lower compressive strength than the recommended 34.5 MPa limit for refrigerated liquefied gas containment [2]. It has been shown that larger aggregates with high porosity and high permeability delay the pore pressure relaxation time, and thus exhibit high stress at the aggregate–matrix interface [34]. This in turn could create microcracks in the matrix shell, where fatigue tensile stress exceeds the fatigue resistance of the matrix. This, in addition to the aforementioned larger pore development mechanism may be responsible for the porosity increase of the air-entrained limestone mixture. Albeit, the air-entrained trap rock mixture with compressive strength lower than the afore-mentioned limit showed good cryogenic frost resistance. This can be explained by the lower total porosity of the air-entrained trap rock mixture compared to the corresponding limestone mixture (Figure 4b). With similar aggregate pore size distribution in concrete, a lower total porosity (or absorption) leads to higher frost resistance as the amount of water expelled from the aggregate into the paste during freezing is limited [30, 34, 35].

The surface relaxivity of the sandstone and river sand samples (Table 2) used as checks for the method agreed well with values reported in the literature. A number of authors have reported surface relaxivity values of ~ 9 µm/s for sandstone [26, 28] and 3 µm/s for silica sand [27]. The estimated surface relaxivities of the concrete mixtures fell within a narrow range, 4.5 – 5.4 µm/s (Table 2) despite the different iron contents of the aggregates (Table 1). This agrees with Dalas et al. [36], who suggested that the amount of paramagnetic species is not a first-order parameter in determining surface relaxivity. These values are similar to the surface relaxivities of synthetic cement hydrates - calcium silicate hydrate (5.5 µm/s), gypsum (6.2 µm/s) and monocarboaluminate (1.65 µm/s) - reported by Dalas et al. [36]. Thus, the surface relaxivities estimated here are apparently the average of the relaxivities of the cement hydrates and the natural rocks used as aggregates. Therefore, with the surface relaxivity values (Table 2), assuming cylindrical pore geometry, the pore diameter of the different pores can be estimated from Figures 2 and 3 using the relation [37]:

$$\frac{1}{T_2} = \rho_2 \left(\frac{S}{V}\right)_{pore} = \rho_2 \frac{2\pi r h}{\pi r^2 h} = \rho_2 \frac{2}{r} = \rho_2 \frac{4}{d}, \quad (3)$$

where, ρ_2 is the T_2 surface relaxivity; $\left(\frac{S}{V}\right)_{pore}$ is the surface-to-volume ratio of the pore; r, h and d, are the radius, height and diameter of the pore, respectively. For example, using equation (3), the estimated pore diameter of the gel pores of the non-air-entrained limestone concrete with T_2 ~ 0.2 ms and surface relaxivity, 4.7 µm/s is calculated as 3.8 nm. For the same concrete, the

capillary pore diameter with T_2 ~ 2 ms (Figure 3a) is calculated as 38 nm. These are within the range of values reported for the gel and capillary pore sizes [38, 39]. Similarly, the pore diameters of the largest voids in the unfrozen lightweight and frozen air-entrained limestone mixtures with T_2 values ~ 1400 ms and 760 ms are calculated as 30 microns and 14 microns, respectively (Figures 3a and 4a). Nevertheless, caution should be taken when converting T_2 data to actual pore sizes since the effect of paramagnetic species on the relaxation is not considered and the pore size is calculated for an equivalent cylindrical pore. In fact, it is common practice to use T_2 as proxy for pore size instead of converting it to actual pore size [16].

3.1 AE data during cryogenic cooling

Figure 5 shows the temperature of the concrete specimens during cooling and warming, together with the AE cumulative hits and cumulative energy. Figure 6 shows the amplitude of the AE hits for the different concrete mixtures. In Figure 6, the saturation amplitude is 99.9 dB due to the 34 dB gain used. Thus, any event greater than 99.9 dB was recorded as 99.9 dB, although the full energy emitted during the event was recorded. The lightweight, air-entrained limestone and sandstone mixtures had the highest number of cumulative hits ranging from ~530,000 (sandstone) to 1.1 million (lightweight), while the trap rock (79,000) and limestone (250,000) mixtures had the lowest cumulative hits (Figure 5c). A comparison of Figures 5a, 5b and 5c shows that the cumulative hits in most of the mixtures started showing a steep increase within the temperature range -20°C to -40°C. The cumulative energy and amplitude plots also showed the same trend, with the latter demonstrating increasing concentrations of high (> 70 dB) amplitude values beyond the above temperature range (Figures 5d and 6). The steep increase in cumulative hits progressed until the temperature range -90°C to -120°C, where there was attenuated increase, which continued until cryogenic temperatures were reached. The steep increase in cumulative hits within the -20°C to -90°C temperature range was occasioned by increase in matrix stresses and microcracking due to ice growth. In addition, since the specimens were tested at near saturation, expansion of the moist concrete, which has been reported to occur within the temperature range, -20°C to -60°C due to ice formation in the capillaries would also cause more AE hits [8, 20]. Further, ice-induced microcracking is reported to cease around -90°C [1, 20], which explains the aforementioned attenuated increase in cumulative hits from -90°C to cryogenic temperatures.

On the other hand, the cumulative energy continued to increase down to cryogenic temperatures before reaching a plateau, for most of the mixtures (Figure 5d). After the attenuated increase as cryogenic temperatures were approached, the cumulative hits and energy of the concrete mixtures further showed a slight increase at the inception of warming to ambient temperature, and reached a plateau thereafter (Figure 5). The same rebound behavior at the inception of

warming is also obvious in the amplitude plots (Figure 6). The lightweight and air-entrained limestone mixtures still indicated significant increase in cumulative hits throughout the warming stage. These mixtures together with the sandstone mixture had higher cumulative energies, ranging from 33 nJ to 290 nJ (Figure 5d). This is in contrast to the other mixtures with lower cumulative energies (7nJ – 16 nJ range), whose hits rate levelled off within the -60°C to -20°C range. This probably explains the relatively higher change in porosity and mean pore size observed in both mixtures in the NMR experiments. Albeit, the increases in cumulative hits during the warming stage did not necessarily correspond to significant increase in cumulative energy since most of such hits had low energy levels.

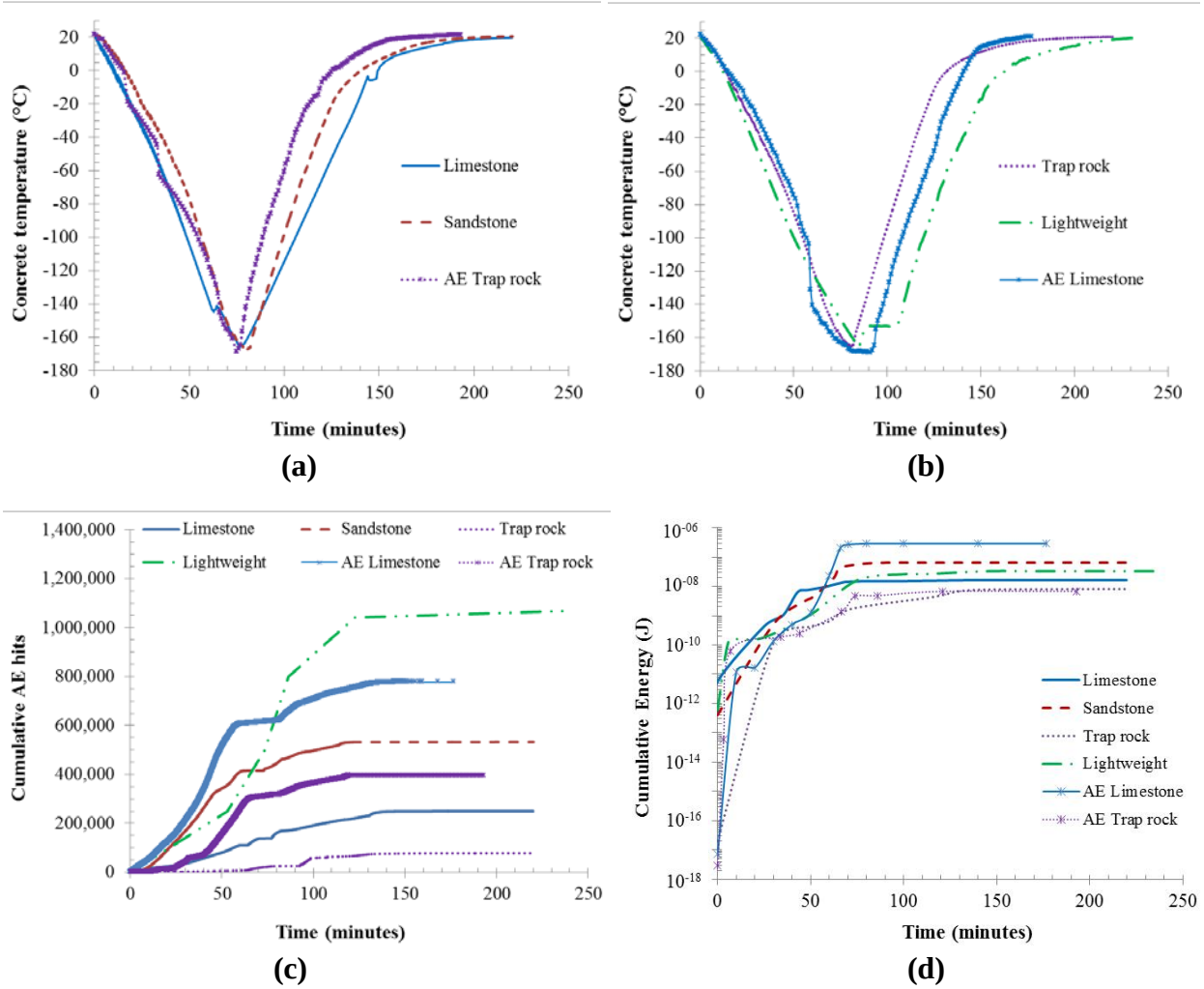

Figure 5. Variation with time of the (a) and (b) temperature (c) cumulative hits, and (d) cumulative energy of the concrete mixtures.

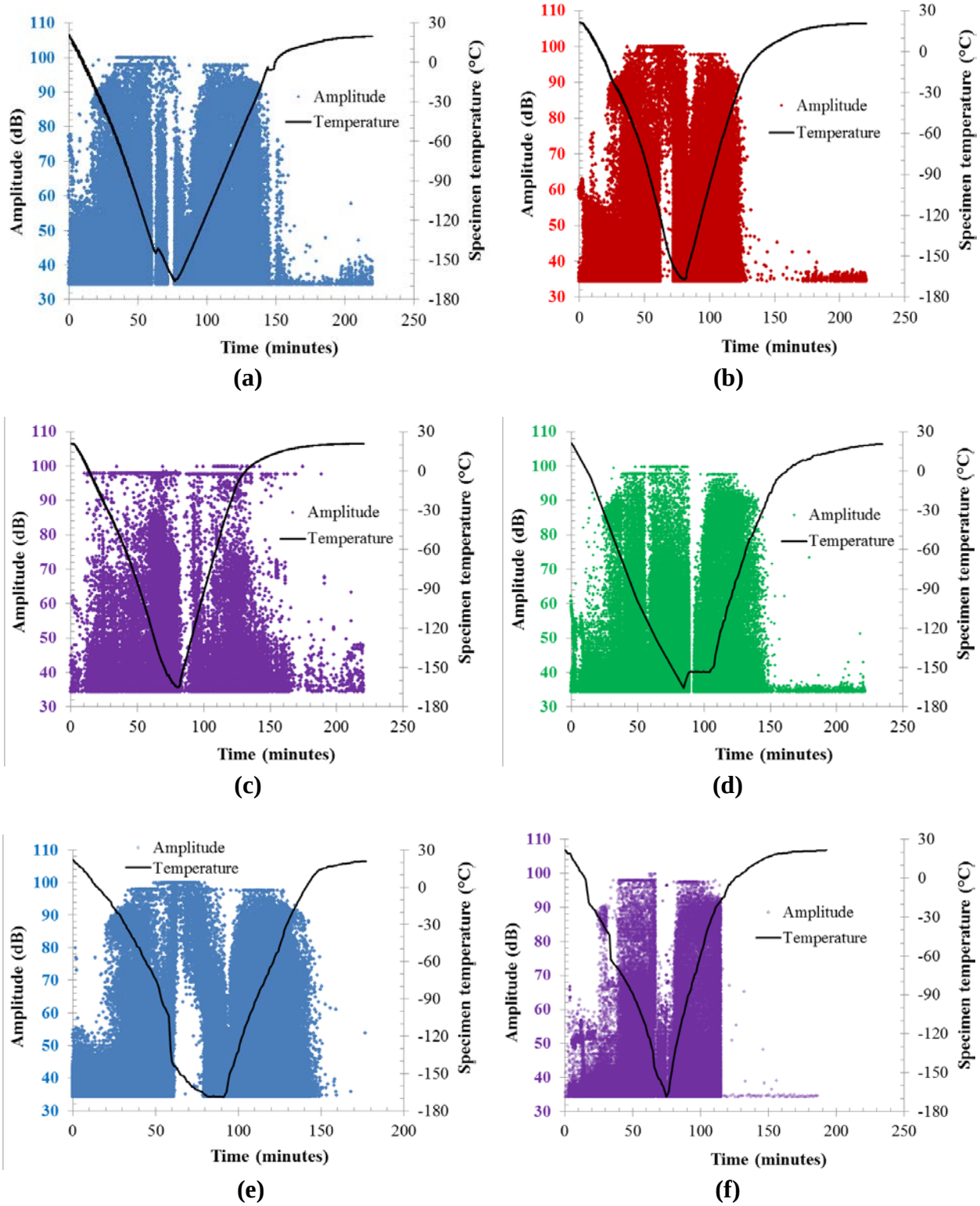

Figure 6. Amplitude of AE events from the non-air-entrained (a) limestone (b) sandstone (c) trap rock (d) lightweight, and air-entrained (e) limestone, and (f) trap rock concrete mixtures during cryogenic cooling and warming.

The increase in cumulative hits during the warming stage can be attributed to stresses in the concrete due to the differential expansion of ice and concrete. Ice expands faster than concrete during the warming stage due to its higher thermal expansion level. Nevertheless, frozen ice then has sufficient free space for expansion without causing marked microcracking [20]. Thus, AE events during the warming stage may have high amplitudes due to the expansive action of frozen ice, but much lower energy as the expansion is less deleterious to the concrete. This probably explains why the cumulative energy-time curves of the concrete mixtures reach a plateau during the warming stage (beyond ~ 80 minutes), although there were quite a number of high amplitude events from cryogenic temperatures until about -20 to 0°C (~ 80 – 150 mins) (Figures 5d and 6). Further, the leveling-off of the hits rate within the -60°C to -20°C range during warming for the mixes with lower cumulative energies could be linked to the aftermath of the higher expansive action of previously frozen water in pores that takes place within that range [20]. Thereafter, ice changes back to water with an attendant reduction in internal stresses and concrete contraction leading to diminished AE hits rate and amplitude levels. Hence, the AE hit-time curves reach a plateau beyond ~ 150 minutes (Figure 5c).

Generally, the results in Figures 5 and 6 show that there are more high amplitude AE activities in concrete during cooling to cryogenic temperature than during warming to ambient temperature. Further, it is also evident from the AE results that as concrete approaches cryogenic temperatures, matrix stresses, and hence the tendency for microcracking, declines significantly. This is a welcome behavior for concrete for direct LNG containment since a slower cooling rate as used in the industry would cause far less damage to the concrete during cooling and once at cryogenic temperatures, further damage is unlikely. Moreover, as previously mentioned, historical evidence suggests that most storage tanks are never emptied once filled with LNG, except for tanks at receiving terminals [1, 20] (thus there would be no warming and re-cooling cycles).

Furthermore, the trend in the AE cumulative hits is very similar to the change in NMR cumulative porosity. The lightweight, air-entrained limestone and sandstone mixtures, which had the highest cumulative hits, also had the highest porosity changes of 3.3%, 1.9% and 1.4%, respectively. Moreover, there was no significant porosity change in the other mixtures with lower cumulative hits. The Spearman's correlation coefficient indicated a very strong positive correlation ($r = 0.90$, $p = 0.015$) between the AE cumulative hits and NMR porosity change. The cumulative energy showed a similar trend, with the mixtures that indicated little or no NMR porosity change emitting the least energies, while those with significant porosity changes emitted more energy (Figures 3, 4 and 5d). There was also a strong positive correlation ($r = 0.81$, $p = 0.05$) between the cumulative energy and NMR porosity change. These show that the association between the cumulative hits and energy recorded during cooling and warming of the concrete mixtures, and the resulting porosity change, is statistically significant. Similarly, a strong

positive correlation and statistical significance also exists in the association between the mean pore size, as determined from the logarithmic mean T_2, and the cumulative hits, as well as the cumulative energy (r = 0.88, p = 0.02, in both cases) (compare Table 2 and Figure 5).

3.2 Microstructural examination

The XRCT images of the concrete mixtures are shown in Figures 7, 8 and 9. The data set consisted of 1014 slices of reconstructed CT images, each with a thickness of ~ 50 microns. The matrix size of the images is 1024 x 1024 pixels with a resolution of 22 microns per pixel in the x-y plane. The rationale behind the millimeter scale of the CT observation is the maximum allowable crack width specified by the ACI 376 code [2]. The code specifies that calculated crack widths within the wall, base slab and roof of the secondary concrete container for refrigerated liquefied gases - there is none for the primary container - shall not exceed 0.012 in. (i.e. ~ 300 micron). A lower value of 0.008 in. (~ 200 micron) was specified within the thermal corner protection embedment zone. These are similar to maximum cracks widths in the order of 250 microns reported for cryogenic concrete [38]. In light of the above, a large representative specimen that takes into account the nominal size of the coarse aggregates was employed such that significant cracking within the concrete could be inspected.

In the slices, with the exception of the lightweight mixture, the aggregates appear as patches with different gray shades, and much brighter than the dark gray shades of the surrounding cementitious matrix. The patches of lightweight aggregates are darker than the surrounding cementitious matrix. Air voids (spherical shapes) and cracks should appear as black or very dark in the images [8]. Five slices are shown for a given concrete mixture, representing the upper, upper middle, middle, lower middle and bottom sections of the core. The slices of a given core shown after freezing are the corresponding, or the closest possible slices to those before freezing in order to facilitate direct comparisons and evaluate the effect of cooling on the cores. This contrasts with the use of replicate cores in a previous related study [8].

There are no visible cracks due to cryogenic cooling in any of the mixtures (Figures 7, 8 and 9). The only evidence of cracking is in the lightweight mixture (Figure 8). The cracks existed across the coarse aggregate before cooling and there is no clear evidence of them being worsened by cooling. This is in contrast to previous findings based on use of replicate cores [8]. This agrees with the position that the damage (microcracks) formed due to cryogenic cooling is very well distributed, with characteristic crack sizes below the resolution of the CT. Thus, large cracks do not tend to form in the concrete cores, but rather well-dispersed microcracks [8]. It can also be seen from the CT images that the lightweight, sandstone and air-entrained limestone mixtures, which indicated significant NMR porosity changes and higher AE cumulative energies,

apparently had more pockets of large pores in their cementitious matrix compared to the other mixtures. Hence, the presence of such large pores (and cracks for the lightweight mixture) makes concrete more vulnerable to frost damage.

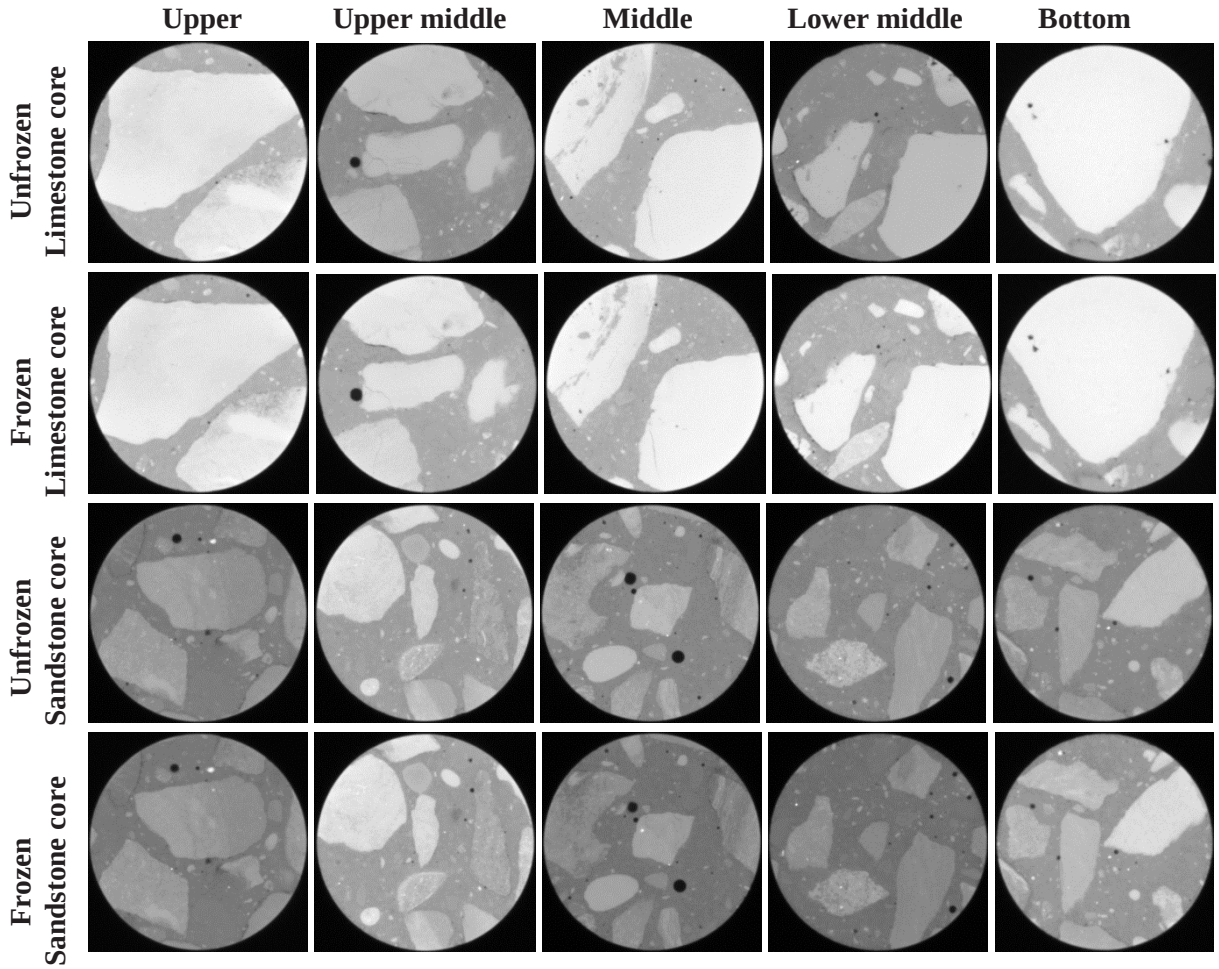

Figure 7. Sample cross-sections of the non-air-entrained limestone and sandstone concrete cores.

1st & 3rd row: Core before cryogenic cooling, 2nd & 4th row: Core after cryogenic cooling.

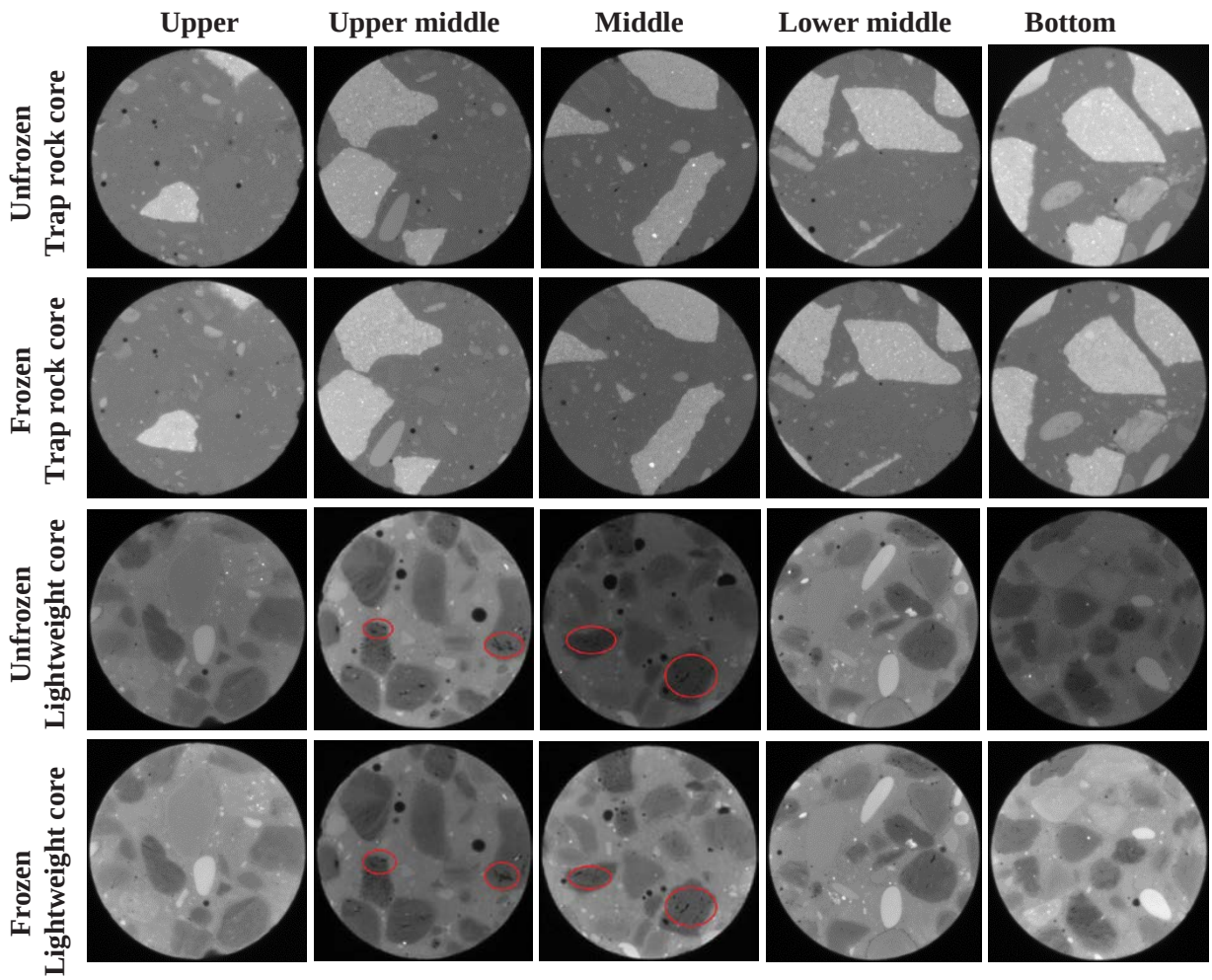

Figure 8. Sample cross-sections of the non-air-entrained trap rock and lightweight concrete cores.

1st & 3rd row: Core before cryogenic cooling, 2nd & 4th row: Core after cryogenic cooling. The ovals in some of the slices indicate cracks.

Attempts were made to investigate cracking in the concrete mixtures using SEM imaging in order to support the XRCT observations. This involved collecting micrographs from the same concrete core before and after cryogenic cooling, as well as on frozen cores stored in thermal insulation material, using the low-vacuum mode. Micrographs were also collected from cores subjected to cryogenic cooling, air-dried and gold-coated, in the high vacuum mode. However, the results of the SEM investigations were inconclusive; hence, they are not shown here. This is probably because the cores were not subjected to polishing steps to achieve conditions appropriate for microstructural evaluation as done in recent studies [40, 41]. Nevertheless, concerns abound with regard to the above. On one hand, the application here involves transport of liquid water or dissolved ions at cryogenic temperatures. Hence, evaluation of the still-frozen

567 microstructure is of interest - this precludes the option of polishing, which would cause surface
568 melting due to frictional heat. On the other hand, in examining specimens allowed to thaw,
569 microcracks formed during cooling could close up and the thawed microstructures would not
570 adequately represent the microstructures of the materials in the frozen state.
571

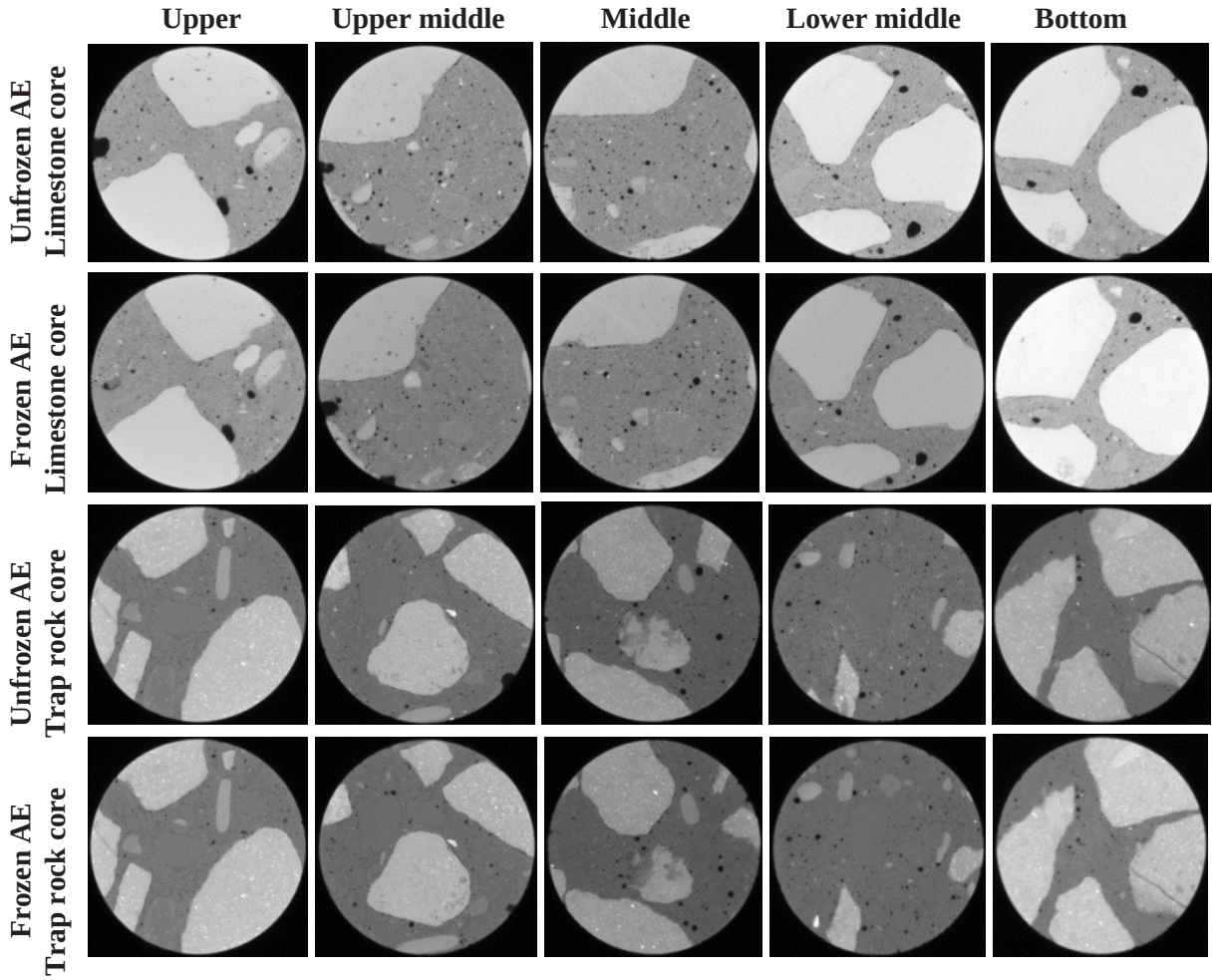

Figure 9. Sample cross-sections of the air-entrained limestone and trap rock concrete cores.

1st & 3rd row: Core before cryogenic cooling, 2nd & 4th row: Core after cryogenic cooling.

572

573 **4. Conclusions**

574 Three non-destructive techniques, namely, NMR, XRCT and AE were deployed for evaluation
575 of different concrete mixtures. The evaluation sought to identify concrete mixtures capable of
576 resisting damage when cooled to cryogenic temperatures typical of LNG storage tanks. NMR
577 signal intensities indicated cumulative porosity increases of 0%, 0.3%, 1.4% and 3.3% in the
578 non-air-entrained trap rock, limestone, sandstone and lightweight concrete mixtures,

respectively. While there were porosity increases of 0% and 1.9% in the air-entrained trap rock and limestone mixtures, respectively. These corresponded to cumulative AE hits ranging from ~79,000 to 1.1 million during cryogenic cooling and warming to ambient temperature. The non-air-entrained trap rock mixture had the lowest, while the lightweight mixture had the highest number of hits. Similarly, AE cumulative energy released ranged from 7 nJ – 290 nJ, with the air-entrained trap rock having the least, and the air-entrained limestone having the highest energy emission. There was a strong positive correlation between AE cumulative hits and energy, and NMR porosity change and mean pore size. XRCT imaging did not show any visible cracking due to cryogenic cooling in the concrete mixtures. It is concluded from the above observations that the generation of interconnected pores and pockets of microcracks during cryogenic cooling and warming occasioned porosity increases in the affected concrete mixtures. Such changes to the pore structure and apparent damage were in the form of microcracks less than the CT's resolution (22 microns).

The above results corroborate previous data on water permeability of the non-air-entrained concrete mixtures. They suggest that the ability of a concrete mixture to resist frost-induced microcracking goes beyond the aggregate CTE and is mainly an interplay between the aggregate CTE, total porosity and pore size distribution. The inferior damage resistance of the air-entrained limestone mixture compared to the corresponding non-air-entrained mixture suggests the importance of the recommended compressive strength of 34.5 MPa in the design of concrete for LNG storage tanks. The compressive strength (29 MPa) of the former was less than the afore-mentioned value. Albeit, this was not a problem in the air-entrained trap rock mixture with 31 MPa compressive strength. These results suggest that trap rock is a highly durable aggregate for the production of concrete for direct LNG containment as it resists frost damage, with or without air-entrainment. Similarly, with the right mixture design, limestone aggregate can also serve as a competing alternative in production of durable concrete for direct LNG containment.

Acknowledgements

This publication was made possible by an NPRP award (NPRP No. 4-410-2-156: Thermal Dilation and Internal Damage of Cryogenic Concrete used for Direct LNG Containment) from the Qatar National Research Fund (QNRF – a member of The Qatar Foundation). The statements made herein are solely the responsibility of the authors. The authors are thankful to Boback Parsaei and Syeda Rahman of Zachry Department of Civil Engineering, Texas A&M University, College Station, USA for their support for the experiments, and Dr. Wubulikasimu Yiming of Texas A&M University at Qatar for assistance with the XRCT and SEM imaging.

References

[1] Kogbara RB, Iyengar SR, Grasley ZC, Masad EA, Zollinger DG. A review of concrete properties at cryogenic temperatures: Towards direct LNG containment. Constr Build Mater. 2013;47:760-70.

[2] ACI. 376-11. Code requirements for design and construction of concrete structures for the containment of refrigerated liquefied gases and commentary. An ACI Standard. American Concrete Institute, Farmington Hills, MI;2011.

[3] ACI. 350-06. Code requirements for environmental engineering concrete structures. American Concrete Institute, Farmington Hills, MI;2006.

[4] Neithalath N, Weiss WJ, Olek J. Predicting the permeability of pervious concrete from non-destructive electrical measurements. Proceedings of the Concrete Technology Forum on Pervious Concrete (in CD-ROM), Nashville, May;2006.

[5] Garboczi EJ. Permeability, diffusivity, and microstructural parameters: A critical review. Cem Concr Res. 1990;20:591- 601.

[6] Blümich B, Perlo J, Casanova F. Mobile single-sided NMR. Prog Nucl Mag Res Sp. 2008;52(4):197-269.

[7] Cnudde V, Boone MN. High-resolution X-ray computed tomography in geosciences: A review of the current technology and applications. Earth-Sci Rev. 2013;123(0):1-17.

[8] Kogbara RB, Iyengar SR, Grasley ZC, Rahman S, Masad EA, Zollinger DG. Relating damage evolution of concrete cooled to cryogenic temperatures to permeability. Cryogenics. 2014;64:21 - 8.

[9] Sagar RV, Prasad BKR. A review of recent developments in parametric based acoustic emission techniques applied to concrete structures. Nondestruct Test Eva. 2012;27(1):47 - 68.

[10] Amitrano D, Gruber S, Girard L. Evidence of frost-cracking inferred from acoustic emissions in a high-alpine rock-wall. Earth Planet Sci Lett. 2012;341:86 - 93.

[11] Stingaciu LR, Weihermüller L, Haber-Pohlmeier S, Stapf S, Vereecken H, Pohlmeier A. Determination of pore size distribution and hydraulic properties using nuclear magnetic resonance relaxometry: A comparative study of laboratory methods. Water Resour Res. 2010;46:W11510. doi:10.1029/2009WR008686.

[12] Bryar TR, Daughney CJ, Knight RJ. Paramagnetic effects of Iron(III) species on nuclear magnetic relaxation of fluid protons in porous media. J Magn Reson. 2000;142:74 – 85.

[13] Bowers MC, Ehrlich R, Howard JJ, Kenyon WE. Determination of porosity types from NMR data and their relationship to porosity types derived from thin section. J Petrol Sci Eng. 1995;13(1):1 - 14.

[14] Lahajnar G, Blinc R, Rutar V, Smolej V, Zupančič I, Kocuvan I, et al. On the use of pulse NMR techniques for the study of cement hydration. Cem Concr Res. 1997;7(4):385 - 94.

[15] Tziotziou M, Karakosta E, Karatasios I, Diamantopoulos G, Sapalidis A, Fardis M, et al. Application of 1H NMR to hydration and porosity studies of lime–pozzolan mixtures. Microporous Mesoporous Mater. 2011;139:16 - 24.

[16] Díaz-Díaz F, de J. Cano-Barrita PF, Balcom BJ, Solís-Nájera SE, Rodríguez AO. Embedded NMR sensor to monitor compressive strength development and pore size distribution in hydrating concrete. Sensors (Basel). 2013;13(12):15985 – 99.

[17] Wang B, Faure P, Thiéry M, Baroghel-Bouny V. 1H NMR relaxometry as an indicator of setting and water depletion during cement hydration. Cem Concr Res. 2013;45:1 - 14.

[18] Promentilla MAB, Sugiyama T. X-Ray microtomography of mortars exposed to freezing-thawing action. J Adv Concr Technol. 2010;8(2):97 - 111.

[19] Monteiro PJM, Kirchheim AP, Chae S, Fischer P, MacDowell AA, Schaible E, et al. Characterizing the nano and micro structure of concrete to improve its durability. Cem Concr Compos. 2009;31(8):577-84.

[20] Krstulovic-Opara N. Liquefied natural gas storage: Material behavior of concrete at cryogenic temperatures. ACI Mater J. 2007;104(3):297 – 306.

[21] Bamforth PB. The structural permeability of concrete at cryogenic temperatures PhD Thesis. UK, Aston University, Available: http://eprints.aston.ac.uk/14275/, [Accessed July 2012]; 1987.

[22] Jehng JY, Sprague DT, Bhattacharja S, Halperin WP. Pore structure evolution and state of pore water in hydrating cement paste at cryogenic temperatures. Engineering, Construction, and Operations in Space V1996. p. 600-7.

[23] ASTM. C39/C39M-14a - Standard test method for compressive strength of cylindrical concrete specimens. West Conshohocken, PA: ASTM International. doi: 10.1520/C0039_C0039M-14A; 2014.

[24] Magritek. Routine core analysis - Porosity measurement. Application Note 1. Available: http://www.magritek.com/wp-content/uploads/2013/12/Magritek-App-Note-001-Porosity-09-2013.pdf. Accessed February 2015. Magritek, Wellington, New Zealand; 2013.

[25] Slijkerman WFJ, Hofman JP. Determination of surface relaxivity from NMR diffusion measurements. Magn Reson Imaging. 1998;16(5–6):541-4.

[26] Liaw H-K, Kulkarni R, Chen S, Watson AT. Characterization of fluid distributions in porous media by NMR techniques. AIChE J. 1996;42(2):538-46.

[27] Hinedi ZR, Chang AC, Anderson MA, Borchardt DB. Quantification of microporosity by nuclear magnetic resonance relaxation of water imbibed in porous media. Water Resour Res. 1997;33(12):2697-704.

[28] Green D. Extracting pore throat size and relative permeability from MRI-based capillary pressure curves. International Symposium of the Society of Core Analysts, Paper No SCA2009-46 Noordwijk, Netherlands2009.

[29] Walker JL, Workman GL. Study acoustic emissions from composites. Draft Final Report submitted to the National Aeronautics and Space Administration, Marshall Space Flight Center, Alabama. Available: https://ia600608.us.archive.org/15/items/nasa_techdoc_19980048926/19980048926.pdf. Accessed February 2015. 1997.

[30] Pigeon M, Pleau R. Durability of concrete in cold climates. Suffolk: E&FN Spon; 1995.

[31] Mehta PK, Monteiro PJM. Concrete: Microstructure, properties, and materials. New York: McGraw-Hill; 2006.

[32] Yuan J, Liu Y, Li H, Zhang B. Experimental investigation of the variation of concrete pores under the action of freeze-thaw cycles by using x-ray CT. Advances in Materials Science and Engineering. 2014;2014:11 pages. doi:0.1155/2014/571357.

[33] Grasley ZC, Scherer GW, Lange DA, Valenza JJ. Dynamic pressurization method for measuring permeability and modulus: II. cementitious materials. Mater Struct. 2007;40(7):711 - 21.

[34] Rahman S, Grasley Z. A poromechanical model of freezing concrete to elucidate damage mechanisms associated with substandard aggregates. Cem Concr Res. 2014;55:88 - 101.

[35] Kaneuji M, Winslow DN, Dolch WL. The relationship between an aggregate's pore size distribution and its freeze thaw durability in concrete. Cem Concr Res. 1980;10(3):433-41.

[36] Dalas F, Korb J-P, Pourchet S, Nonat A, Rinaldi D, Mosquet M. Surface relaxivity of cement hydrates. J Phys Chem C. 2014;118(16):8387-96.

[37] Cohen MH, Mendelson KS. Nuclear magnetic resonance and the internal geometry of sedimentary rocks. J Appl Phys. 1982;53:1127-35.

[38] Van der Veen C. Properties of concrete at very low temperatures: A survey of the literature. The Netherlands: Delft University of Technology, Report 25-87-2. Available: http://repository.tudelft.nl/view/ir/uuid%3Af4175338-4cc3-434e-9046-50769311025d/; 1987.

[39] Haynes JM. Determination of pore properties of constructional and other materials. Mat Constr. 1973;6(3):169-74.

[40] Shaikh FUA, Supit SWM, Sarker PK. A study on the effect of nano silica on compressive strength of high volume fly ash mortars and concretes. Mater Des. 2014;60:433 - 42.

718 [41] Das S, Kizilkanat A, Neithalath N. Crack propagation and strain localization in metallic
719 particulate-reinforced cementitious mortars. Mater Des. 2015;79:15 - 25.

720

721